30th AIAA Applied Aerodynamics Conference
25 - 28 June 2012, New Orleans, Louisiana

AIAA 2012-2795

Aerodynamics of a Swept Wing with Ice Accretion at Low Reynolds Number

Jeff M. Diebold*, Marianne C. Monastero† and Michael B. Bragg‡
University of Illinois at Urbana-Champaign, Urbana, IL 61801

This paper discusses the use of several experimental techniques to investigate the performance and flowfield of a swept wing with leading-edge ice at low Reynolds numbers. Force balance measurements were made over a range of angles of attack and Reynolds numbers. Surface oil visualization and pressure sensitive paint were used to investigate the flow over the surface of the wing, while five-hole probe wake surveys were used to investigate the wake. The flowfield of the iced swept wing was dominated by a leading-edge vortex that formed at low angles of attack due to separation from the tip of the ice shape, while for the clean wing a vortex did not form until higher angles of attack. The effect of Reynolds number on the performance and flowfield was also investigated.

1.0 Introduction

Aircraft icing has received significant attention from researchers over the past several decades. To date, the vast majority of aerodynamic icing research has focused on the aerodynamic impact of ice accretions on two-dimensional airfoils.[1,2,3] Bragg et. al.[4] in 2005 reviewed the literature of iced airfoil aerodynamics with a focus on the physics of iced airfoil flowfields. Lynch and Khodadoust[5] in 2001 reviewed the effects of ice on aircraft aerodynamics. Both of these reviews cited over 100 different references, indicating the vast amount of research done in the field. Unlike airfoils, the effects of icing on the aerodynamics of three-dimensional wings and particularly swept wings have received little attention. Papadakis et. al.[6,7] studied the effects of several different ice accretions on a swept wing. They measured decreases in maximum lift as high as 93.6% and increases in drag as high as 3500%. Broeren et. al.[8] studied the aerodynamic effects of simulated ice accretions on a generic transport model. In addition to force balance measurements, insight into the flowfield was gained via surface oil flow visualization. Khodadoust and Bragg[9] performed surface oil flow visualization and helium bubble visualization for a straight and swept wing with simulated ice accretion and Bragg et. al.[10] performed LDV measurements on the same model.

A common feature of the few swept wing icing studies that have been conducted is the low Reynolds number of the experiments. The research discussed so far spanned a Reynolds number range of approximately 0.24×10^6 to 1.8×10^6. It is difficult to obtain high Reynolds number performance data on swept wings due to the small scale of most tunnels and the limited availability and cost of pressure tunnels. Currently there is interest in obtaining high Reynolds number data on swept wings with ice accretions to better understand the flow at near-flight conditions. This paper, although still at low Reynolds number, is being conducted toward that goal by developing the experimental tools to study the effect of ice accretion on swept wing aerodynamics. Thus this paper will discuss the experimental techniques in the context of utilizing them to better understand the aerodynamics of a highly swept, high aspect ratio wing with a simple ice accretion at low Reynolds numbers. The data presented here is not intended to be representative of the aerodynamic performance of the wing at high Reynolds numbers, but rather its purpose is to demonstrate how these techniques can be applied to better understand the aerodynamics of a swept wing with a leading-edge ice accretion.

2.0 Experimental Methods

2.1 Model

The model used in this investigation was a modified version of the Common Research Model (CRM). The CRM was designed by Vassberg et. al.[11] for the 4th AIAA Drag Prediction Workshop. The CRM was designed to represent a typical wide body swept wing commercial aircraft. The geometry of the CRM, as well as experimental and computational data, is publically available making it a good choice for the baseline geometry. The wing of the CRM has a modern transonic supercritical airfoil and was designed for well-behaved performance with and without

* Graduate Research Assistant, Department of Aerospace Engineering, Member AIAA.
† Graduate Research Assistant, Department of Aerospace Engineering, Member AIAA.
‡ Professor of Aerospace Engineering, Executive Associate Dean for Academic Affairs, Fellow AIAA.

the nacelle/pylon group. The original CRM has an aspect ratio of 9, LE sweep of 35 deg., a taper ratio of 0.275 and 8 degrees of twist from the root to the tip. For the experiments at the University of Illinois the CRM wing was modified to reduce model cost and improve structural integrity due to the small size of the model. These modifications included the removal of dihedral, linearizing the twist distribution and increasing the airfoil thickness by 20% around the mean camber line. Table 1 summarizes the geometric features used in this study as well as the original CRM. The chord was measured in the streamwise direction On the original CRM the first 10% of the span is located within the fuselage of the aircraft and this area was not used for the current model thus reducing the aspect ratio and increasing the taper ratio.

Table 1. Comparison of CRM and Wind Tunnel Sizing.

	Illinois Model	CRM
AR	8.3	9.0
LE Sweep	35	35
MAC (ft)	0.5167	11.98
Max Thickness (ft)	0.1458	4
Min Thickness (ft)	0.0241	0.85
Semispan (ft)	2.1	96.4
Taper Ratio	0.296	0.275

The exterior shell of the model was manufactured using stereolithography (SLA) and was supported by a steel frame. The shell consists of three components; an upper surface, lower surface and leading-edge. A clean and an iced leading-edge were built and designed to be easily interchangeable during testing. The completed model is shown in Fig. 1. Unfortunately, the quality of the model near the seams of the various SLA pieces was not ideal. In these areas the SLA was relatively thin and warped slightly, causing small gaps and steps along the seams. The gaps and seams were smoothed using modeling clay. There were 120 surface pressure taps in five streamwise oriented rows. The pressure taps were also used to calibrate the pressure sensitive paint.

2.2 Ice Shape Simulation

For these preliminary experiments a simple leading-edge ice shape simulation was generated. It should be noted that the goal was not to develop an accurate ice shape, but rather a simple representative simulation that would have a substantial impact on the aerodynamics. The ice shape was produced using the following procedure based on a 2D strip theory analysis discussed by Potapczuk et. al.[12] First, a potential flow solution of the wing was generated using XFLR5.[13] Several airfoil sections normal to the leading-edge were chosen and the potential flow solution was used to obtain lift coefficients for these sections. The sectional lift coefficients and the corresponding airfoil section were input into XFOIL[14] to determine the local angle of attack. This local angle of attack and the airfoil section were then input into NASA's LEWICE 3.0, which is a 2D ice accretion prediction code. The output from LEWICE was 2D ice shapes corresponding to several spanwise locations along the leading-edge of the wing. Table 2 lists the icing conditions used and Fig. 2 shows the ice shape cross-sections at the root, midspan and tip. In the method described by Potapczuk et. al.[12] the sweep angle is accounted for by using the velocity component normal to the leading-edge. Therefore the velocity listed in Table 2 corresponds to a wing with 35º sweep and a freestream velocity of 250 mph. These ice shape cross-sections were then lofted together to create a continuous three-dimensional ice shape simulation. The icing conditions were chosen to produce a reasonably sized ice shape.

Table 2. Icing conditions used as input to LEWICE 3.0.

Time (sec)	V_∞ (mph)	LWC (g/m^3)	δ (μm)	Temp (F)
2400	205	1	30	20

2.3 Wind Tunnel and Force Balance

Experiments discussed in this report were carried out at the University of Illinois Low Speed Wind Tunnel. The subsonic, open-return wind tunnel has a 3-ft by 4-ft test section and a maximum speed of approximately 235 ft/sec. As can be seen in Fig. 1, the model was mounted in the semispan configuration. The semispan of the model was chosen to minimize the blockage and to obtain the highest Reynolds number possible for the given aspect ratio. The model was connected to the force balance located directly beneath the tunnel floor. The three component force balance measured lift, drag and pitching moment about the quarter chord of the mean aerodynamic chord. Force balance measurements were corrected for tunnel wall effects using the methods discussed in Barlow et. al.[15] The use

of a half fuselage or standoff was considered to minimize the effect of the floor boundary layer; however, the purpose of this study was only to assess the relative effect of the ice shape and it was therefore decided to forego the use of such a device. Force balance measurements were made over a range of angles of attack at Reynolds numbers based on the mean aerodynamic chord of $3x10^5$, $6x10^5$ and $7.8x10^5$.

2.4 Surface Oil Flow

Flow visualization was conducted using the surface oil flow technique. First, the model was covered with self-adhesive contact paper. The black contact paper protected the model surface as well as the pressure taps and provided a contrasting background. The model was covered with a thin layer of motor oil followed by a mixture of mineral oil and oil based fluorescent dye. The dye mixture was applied with an airbrush to ensure an even coating. The tunnel ran for one to three minutes, and then fluorescent lights were placed inside the tunnel. Images were taken at several different angles of attack at Reynolds numbers of $3x10^5$ and $6x10^5$.

Surface oil flow visualization is a relatively simple method that allows visualization of the time averaged flow over the surface of the model. By analyzing the oil flow pattern it is possible to locate areas of separated and reversed flow as well as leading-edge vortices on a swept wing. This information can be used to better understand the results of the force balance and surface pressure measurements.

2.5 Pressure Sensitive Paint

Pressure sensitive paint (PSP) was applied to the upper surface in order to obtain the global pressure field. Liu and Sullivan provide a detailed review of the PSP technique.[16] In this study, the PSP technique used was based on the method described by Bell[17] using the Innovative Scientific Innovations Incorporated (ISSI) UniFIB Pressure Sensitive Paint. A brief description of the method is given here.

The model was first covered with the same contact paper used for the oil flow. A white primer was applied followed by application of the UniFIB paint with an airbrush. Excitation light was supplied by an ultraviolet LED lamp and emitted light was captured by a low noise CCD camera. For each angle of attack a set of 50 wind-on and wind-off images were acquired using an exposure time of 0.25-0.3 seconds. Each image set was then averaged and a background image was subtracted to remove any ambient light. Due to model deformation it was necessary to align each wind-on image with the corresponding wind-off image. The pressure taps were used to define a polynomial transformation to align the images using ISSI's PSP post processing software, OMS Lite. OMS Lite was then used to calculate the intensity ratio of the wind-off to the wind-on images. The ratio accounts for non-uniformities in illumination and paint application. During data acquisition surface pressures were measured at the upper surface pressure taps and used to calibrate the paint. The average intensity values around each tap were plotted against the measured pressures. This relationship was then applied to the images to determine a continuous pressure coefficient distribution over the surface. Due to viewing limitations it was necessary to take separate images for the inboard and outboard sections. To combine the separate images, the 2D and 3D tap coordinates were used to perform a Direct Linear Transform that mapped the 2D images to the 3D model surface, as is described by Cattafesta and Moore.[18] It should be noted that work is still under development in an attempt to further improve the joining of the inboard and outboard images.

2.6 Wake Survey

Wake surveys were performed using an Aeroprobe Corp. model PS5-C318-152 five-hole probe. The probe tip was conical with a base diameter of 0.125-in., the tip contained one central pressure port and four evenly space peripheral ports. Using a proper calibration, the five measured pressures could be used to determine the total and static pressure as well as all three components of velocity. In this report the wake survey results will be used as an additional flowfield diagnostic technique. In a future report, the wake survey data will be used to further investigate the lift and drag on the wing using the method discussed by Brune.[19] This application of the wake data is currently being developed.

Measurements were made in a plane located at $2x/b = 0.8$ downstream of the trailing-edge of the tip. The survey extended from $2y/b = 0.156$ to $2y/b = 1.101$ in the spanwise direction, and from $2z/b = -0.207$ to $2z/b = 0.2$ in the normal direction. The portion of the wake less than $2y/b = 0.156$ was not surveyed in order to avoid the influence of the floor boundary layer. A variable stepsize was used depending on the probe location. The stepsizes are summarized in Table 3. The wake measurements presented in this paper were taken at a Reynolds number of $6x10^5$. The calibration procedure and data reduction process is described in detail by Diebold.[20]

Table 3 Vertical and Horizontal probe stepsize used for wake survey.

	Vertical Step Size (Δy)		Horizontal Step Size (Δz)	
Region	$0.15 \leq 2y/b < 0.9$	$2y/b \geq 0.9$	$\|2z/b\| > 0.1$	$-0.1 \leq 2z/b \leq 0.1$
Stepsize (2/b)	0.0198	0.0099	0.0149	0.0099
Stepsize (in.)	0.5	0.25	0.375	0.25

3.0 Results and Discussion

3.1 Force Balance Results

The results of the force balance measurements for the clean and iced wing, corrected for tunnel wall effects, are shown in Fig. 3. The influence of the ice on the aerodynamic performance was significant. Over the Reynolds number range tested the average increase in C_{Dmin} due to the ice shape was 78.7% with a maximum of 85.8% occurring at Re = $3x10^5$. At a lift coefficient of 0.5 the average increase in drag of the iced wing was 58.3% with a maximum increase of 68% occurring at $3x10^5$.

The stalling characteristics of the wing can be inferred from the balance data. In all cases the wing exhibited a gentle stall beginning at the tip. Tip stall is indicated by the increase in pitching moment (nose-up), which is due to the forward movement of the center of pressure as the lift from the tip section decreased. The presence of the ice shape did not dramatically change the stalling characteristics of the wing. While the behavior of the lift curve after stall differed from the clean wing, a gentle tip stall still occurred, although the increase in pitching moment was not as large as in the clean case.

Due to the lack of a true maximum C_L, the stalling angle of attack (α_{stall}) is defined here as the angle of attack at which the pitching moment is minimum. While this point may not coincide with the maximum lift coefficient, it does correspond to an unstable break in pitching moment and a break in the drag curve. This increase in pitching moment is due to tip stall as discussed above. The angles of attack and lift coefficients corresponding to the minimum pitching moment for the clean and iced wing are summarized in Tables 4 and 5. Examining Fig. 3 it can be seen that α_{stall} also marks a change in the lift curve slope and at angles past α_{stall} the drag coefficient increased rapidly. The decrease in the lift curve slope was due to a change in the aerodynamic performance of the outboard sections of the wing. The ice decreased the stalling angle by 2.65º for the lowest Reynolds number and 4.65º at the highest. In addition, $C_{L,Stall}$ was reduced by an average of 38.4%. The data in Tables 4 and 5 also show a reduction in the influence of the Reynolds number for the iced wing. This will be discussed further in Section 3.3.

Table 4 α_{Stall} and $C_{L,Stall}$ for the clean wing. (Stall defined at $C_{M,min}$)

Re ($x10^5$)	α_{Stall}	$C_{L,Stall}$
3.0	8.60	0.70
6.0	9.65	0.78
7.8	10.2	0.82

Table 5 α_{Stall} and $C_{L,Stall}$ for the ice wing. (Stall defined at $C_{M,min}$)

Re ($x10^5$)	α_{Stall}	$C_{L,Stall}$
3.0	5.95	0.53
6.0	5.98	0.56
7.8	5.98	0.57

3.2 Flowfield

The remainder of this paper will use the results of various experimental methods to discuss the flowfield features of the clean and iced swept wing. The goal is to obtain a better understanding of how the ice influences the flowfield and thus the performance of the wing. Surface oil flow visualization and pressure sensitive paint results for the clean wing over a range of angles of attack are shown in Fig. 4. For the oil and PSP images the span from approximately the root to 10% span is not shown. At α = 3.36º there were several oil accumulation lines along the leading-edge that resulted from the small steps in the surface of the model where the removable leading-edge met the upper surface. Near the tip at the lower angle of attack a separated region formed near mid-chord. At α = 5.48º, 7.59º and 8.62º the oil accumulation lines resulting from the leading-edge/upper surface discontinuity had disappeared over most of the wing and the oil accumulation line present near the leading-edge was a result of laminar separation. Though difficult to see, when the separation was followed by reattachment, the flow in the

recirculating region was three dimensional due to the spanwise pressure gradient. Therefore the flow reattached to form a small leading-edge vortex. The leading-edge vortex formed at these angles of attack could be considered the 3D counterpart to laminar separation bubbles on airfoils. It will be seen that a significantly different leading-edge vortex forms when stall occurs. From the PSP results it can be seen that as the angle of attack increased the suction peak increased as did the chordwise extent of the low pressure region. This led to an increase in the spanwise pressure gradient and a significant amount of spanwise flow in the boundary layer near the trailing-edge which was visible in the oil flow.

Oil flow and PSP results for the iced wing over a range of angles of attack are shown in Fig. 5. Note the different scale used for the PSP images compared with Fig. 4. Beginning at low angles of attack the flow separated at the tip of the ice shape and rolled up to form a leading-edge vortex which can be seen in the oil flow. The low pressure region seen in the PSP closely followed the reattachment line of the vortex and was due to the high rotational velocities within the vortex. The modified pressure distribution led to a decrease in lift, an increase in drag and a forward shift of the center of pressure resulting in an increased pitching moment.

The surface topology of the leading-edge vortex was characterized by a primary separation line at the leading-edge, a reattachment line and a secondary separation line; these features are shown in Fig. 6. For the iced wing, the primary separation line was the tip of the ice shape. The separated flow rolled up to form a vortex which pulled fluid down to the surface forming a reattachment line marking the division between flow in the upstream and downstream direction. The fluid under the vortex, flowing in the upstream direction, initially experienced a favorable pressure gradient as the center of the vortex was approached. After passing under the center of the vortex an adverse pressure gradient forced the boundary layer to separate at the secondary separation line. A similar flowfield was observed by Broeren et. al.[8] on the swept wing of a generic transport model with simulated ice, and by Poll on swept wings with sharp leading-edges.[21]

The leading-edge vortex also contained similarities to the 2D separation bubble behind a horn ice shape on airfoils. On an airfoil, the flow separates at the tip of the horn, the shear layer then transitions and turbulent mixing promotes reattachment. Below the separated shear layer is a recirculation zone where the pressure is nearly constant until the shear layer transitions. As the angle of attack increases the reattachment point of the 2D bubble moves downstream and can grow as large as 40% of the chord.[22] Figure 7 shows the oil flow for the iced wing at $Re = 3x10^5$ over a range of angles of attack with the reattachment line highlighted. Note the oil flow for $Re = 3x10^5$ is nearly identical to the oil flow for $Re = 6x10^5$ shown in Fig. 5. It can be seen that as the angle of attack increased the reattachment line moved downstream indicating that the vortex had grown similar to a 2D bubble.

Unlike in the 2D bubble, however, the vortex is inherently three dimensional. There are numerous factors which influence the leading-edge vortex along the span including the local size of the ice shape relative to the chord, the local angle of attack and the spanwise pressure gradient which is responsible for moving flow within the vortex from the inboard to the outboard sections. These mechanisms and others work to control the size of the vortex and therefore the reattachment location. In Figs. 5 and 7 it can be seen that as the angle of attack increased, which increased three dimensional effects, the reattachment line became increasingly nonlinear as seen by several kinks in the line. Similar kinks were observed by Poll[21] and were attributed to vortex bursting. The most significant change in the reattachment line, located at approximately $2y/b = 0.75$, marks an abrupt change in the oil pattern between the inboard and outboard sections. This feature first appeared at $\alpha = 3.36^\circ$ and remained at the higher angles of attack. The PSP results, in Fig. 5, show that outboard of this kink the chordwise extent of the low pressure region increases significantly indicating a change in the load distribution. As the vortex grew the secondary separation line did not appear to move.

The five-hole probe wake surveys were also used to compare the flowfield of the clean and iced wing. Contours of axial velocity with transverse velocity vectors in the wake of the clean and iced wing are shown in Fig. 8a and 8b respectively for $\alpha = 3.36^\circ$ and $Re = 6x10^5$. From the figures, it can be seen that the wake of the iced wing was significantly thicker than that of the clean wing; a result of the higher drag of the iced wing. The tip vortices of the two wakes contained several differences. First, the tip vortex of the iced wing was less distinct from the rest of the wake than the clean tip vortex. This was likely the result of increased mixing caused by the higher turbulence in the iced wake as well as the entrainment of separated flow into the vortex. In addition, the tip vortex of the iced wing contained a larger region of significant axial velocity deficit consistent with the higher drag measurements. Finally, the velocity vectors indicate reduced rotational velocities in the vortex of the iced wing. Maximum transverse velocities within the vortex of $0.16U_\infty$ and $0.12U_\infty$ were measured in the clean and iced wing respectively. Smaller rotational velocities indicate a weaker vortex which is consistent with the smaller lift coefficient of the iced wing at $\alpha = 3.36^\circ$.

Figures 9a and 9b show the wake of the clean and iced wing at 8.62° and 5.46° respectively. These angles of attack are just prior to stall for each wing. For the clean wing, compared to the lower angle of attack shown in

Fig. 8a, the wake was thicker and the maximum rotational velocities in the tip vortex had increased up to $0.3U_\infty$, but the structure of the wake had not changed significantly. For the iced wing however there were substantial differences in the structure of the wake between $\alpha = 3.36^\circ$, Fig. 8b, and $\alpha = 5.46^\circ$, Fig. 9b. At the higher angle of attack a second vortex centered at approximately $2y/b = 0.74$ had formed. The location of this vortex in the wake was slightly inboard of the major kink in the reattachment line on the outboard portion of the wing shown in Fig. 7 for $\alpha = 5.46^\circ$. The flow feature responsible for the abrupt change in the oil flow pattern results in a shed vortex visible in the wake.

The post stall flowfield of both the clean and iced wing was dominated by a leading-edge vortex. Figures 10a and 10b show the oil flow pattern and PSP images for the stalled clean and iced wing, respectively, at $Re = 6x10^5$. Note that for the PSP images, only the inboard sections of the wing are shown. The image processing method was unable to properly align the wind-on and wing-off images due to the large deflections at the tip. The vortex on the clean wing began near midspan and quickly increased in diameter as it turned away from the leading-edge and left the wing at approximately 70% span. The PSP shows high suction at the initiation of the vortex and the pressure rises along the axis of the vortex as the diameter increased and the rotational velocities decreased. The oil flow shows that outboard of the vortex the near surface flow was nearly all reversed. This was consistent with the pitching moment behavior which indicated tip stall. Inboard of the vortex the flow was attached and there was significant spanwise flow near the surface due to the large spanwise pressure gradient caused by the vortex.

The leading-edge vortex that occurred post stall on the iced wing, see Fig. 10b, was significantly different from the leading-edge vortex formed at lower angles of attack. At low angles the leading-edge vortex occupied most of the span, the flow fully reattached behind the vortex and the diameter of the vortex did not change significantly along the span, see Figs. 5 and 7. The leading-edge vortex of the iced wing began closer to the root than the clean wing and then grew at a steady rate until approximately midspan where it began to curve away from the leading-edge and left the wing near 60 to 70% span. Inboard of where the vortex began to curve the flow remained attached and the oil flow and PSP images were similar to the images at the lower angles of attack. As on the clean wing, the PSP shows low pressures at the initiation of the vortex and an increase in pressure as the diameter of the vortex increased. In the center of the span of the iced wing oil flow showed reversed flow along the surface. Interestingly, the abrupt change in the oil flow pattern visible at $\alpha = 5.46^\circ$ near $2y/b = 0.75$ was still visible post stall in Fig. 10b. Outboard of this change a reattachment line is visible in the oil indicating the flow is still attached on the aft portion of the chord near the tip.

Figures 11 and 12 show the surface oil flow and the wake surveys for the clean and iced wing post stall with several relevant features labeled. For the clean wing, Fig. 11, inboard of the reattachment line the flow remained attached and the structure of the wake in this region was not significantly different than the wake at lower angles of attack. Outboard of the reattachment line the structure of the wake changed significantly. The leading-edge vortex, clearly visible in the wake, contained a significant axial momentum deficit located near the center of rotation. In between the leading-edge vortex and the tip vortex was a large region of low axial momentum with a thickness of nearly 30% of the span in both the y and z direction. The size of the low momentum region in the tip vortex increased significantly from $\alpha = 8.62^\circ$, Fig. 8a.

As was the case for the clean wing, the flow remained attached inboard of the leading-edge vortex on the iced wing and the wake in this region, shown in Fig. 12, resembled the wake at lower angles of attack. Outboard of the reattachment line the wake differed from the clean wing in several ways. The low momentum region of the iced wing was not as large as for the clean wing although it should be pointed out the two wings were no longer at the same angle of attack. As was the case for the low angles of attack, the low momentum region of the tip vortex was not as distinct from the rest of the wake as for the clean wing. It is also interesting to point out that neither the leading-edge vortex nor the tip vortex appeared to be aligned with the freestream. This is indicated by the elliptical rather than circular patterns of the streamlines and the low momentum region not coinciding with the center of rotation.

3.3 Reynolds Number Effects

The force balance data, summarized in Tables 4 and 5, showed a reduction in the Reynolds number effects due to the presence of the ice shape. For the clean wing, as the Reynolds number increased from 3×10^5 to 6×10^5, α_{Stall} and $C_{L,Stall}$ increased by approximately 12.2% and11.4% respectively. The difference in lift could be attributed to a difference in slope beginning at an angle of attack of approximately 2° where the slope of the lower Reynolds number case decreases. As the Reynolds number is increased from 6×10^5 to 7.8×10^5, increases in α_{Stall} and $C_{L,Stall}$ of 5.6% and 5.1%, respectively, were observed.

As can be seen from Table 5 the presence of the ice shape reduces the effect of Reynolds number especially when considering α_{Stall} of the iced wing, which was nearly unaffected by Reynolds number. As the Reynolds number

increased from 3 x10^5 to 6 x10^5, $C_{L,Stall}$ of the iced wing increased by 5.6% whereas $C_{L,Stall}$ of the clean wing increased by 12.2% for the same change in Reynolds number. From a Reynolds number of 6 x 10^5 to 7.8 x 10^5 $C_{L,Stall}$ of the iced wing only increased by 1.7%. The decreased influence of the Reynolds number when an ice shape is present has been observed on airfoils and is due to the geometry of the ice shape fixing the separation point.[4] It is important to restate that the experiments discussed here were performed at very low Reynolds numbers. While the trend of decreased Reynolds number influence on iced airfoils was demonstrated at higher Reynolds numbers, it is unknown if the same is true for swept wings. In addition, all tests were performed in an atmospheric wind tunnel and, therefore, the Mach number could not be held constant.

The effect of the Reynolds number can also be seen in the flowfield. Figure 13 compares oil flow for the clean wing from 2y/b = 0.68 to the tip for $\alpha = 3.36^o$ at Reynolds numbers of 3x10^5 and 6x10^5. It should be restated that the oil accumulation lines near the leading-edge were due surface imperfections as discussed above. At the lower Reynolds number there is a region of low shear beginning near midchord. The flow then separates, although it is difficult to determine where separation begins. A reattachment line is visible near the trailing-edge and secondary separation is indicated by the oil accumulation line. At the higher Reynolds number the region of low shear and separation near the trailing-edge can be seen, but the spanwise and chordwise extent of this feature had decreased. Figure 14 shows the Reynolds number effect on the iced wing tip region for the same angle of attack. Here very little difference can be seen when the Reynolds number increased.

Figure 15 shows a close up of oil flow for the clean wing from $0.625 \leq 2y/b \leq 0.925$ at $\alpha = 7.6^o$ for Reynolds numbers of 3x10^5 and 6x10^5. At this angle of attack the lift is increased by 3.9% and the drag is decreased by 7.0% as a result of the increase in Reynolds number. From Fig. 15 it can be seen that this change in performance is due to the presence of a leading-edge vortex that covered most of the span at the lower Reynolds number but did not occur at the high Reynolds number. The reattachment line is difficult to see in the figure and the first oil accumulation line nearest the leading-edge was due to primary separation while the second was due to secondary separation.

Figure 16 shows a close up of oil flow for the iced wing from $0.45 \leq 2y/b \leq 0.75$ at $\alpha = 5.46^o$ for the same Reynolds number increase as in Fig. 15. The surface flows at the two Reynolds numbers are nearly identical, which is consistent with the similar performance indicated by the force balance data. The most significant difference was that the location of secondary separation was further upstream at the higher Reynolds number. This is not surprising given that at higher Reynolds numbers boundary layers are less susceptible to separation.

4.0 Conclusions

This paper presented the results of several experimental methods used to investigate the aerodynamic performance and flowfield of a modern swept wing with leading-edge ice. The experiments were conducted at low Reynolds number, but provide some potential tools for understanding the effects of ice at higher Reynolds numbers. Force balance data showed the ice had a significant effect on the performance of the wing. Pressure sensitive paint and surface oil flow visualization showed that the performance penalties were the result of the separated flowfield behind the ice shape. While the iced swept wing flowfield contained some similarities to the two dimensional flow behind an iced airfoil, three dimensional effects played a dominant role. This was especially apparent beyond stall due to the formation of a leading-edge vortex that grew quickly to a size comparable to the local chord before leaving the wing near midspan. This vortex, which formed on the clean wing as well, was clearly visible in the results of five-hole probe measurements made in the wake. The surface oil flow method showed that outboard of the leading-edge vortex the flow near the surface was mostly in the upstream direction indicating the region had stalled. The flow inboard of the vortex remained attached and continued to produce lift and as a result both the clean and iced wing underwent a gentle stalling process. The effects of Reynolds number were also investigated and it was found that the presence of the ice shape reduced these effects. Future work will be aimed at improving the various experimental techniques utilized in this report as well as exploring new methods to investigate the aerodynamics of the swept wing with ice and improve our understanding of this flow.

Acknowledgements

This work was supported under grant DOT FAA 10-G-004. The authors would like to acknowledge the contribution of their technical monitor Dr. Jim Riley of the FAA Technical Center. Thanks is also due to Joe Bottalla and Andrew Mortonson for their work on the design of the swept wing model, as well as Paul Schlais for his assistance in carrying out the various wind tunnel experiments.

Fig. 1 Wind tunnel model.

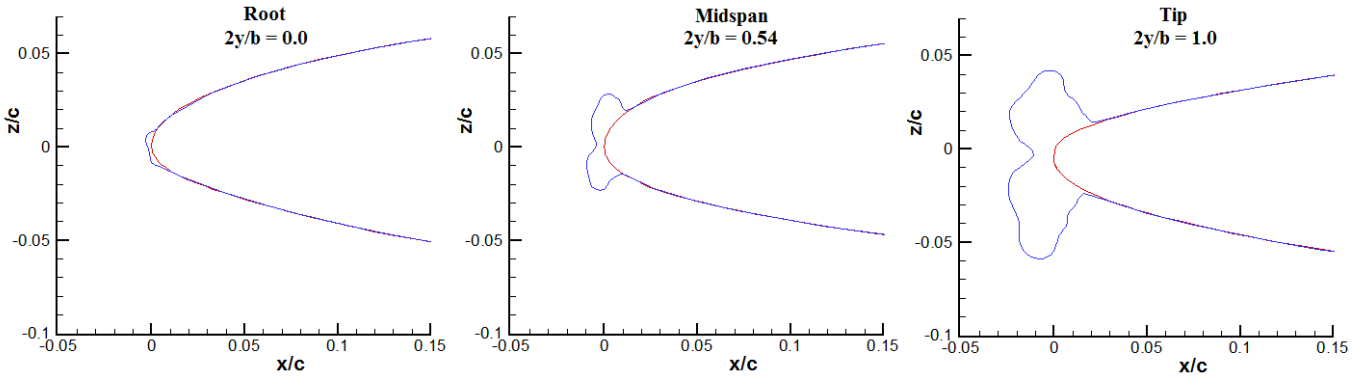

Fig. 2 Ice shape cross-section at several spanwise locations.

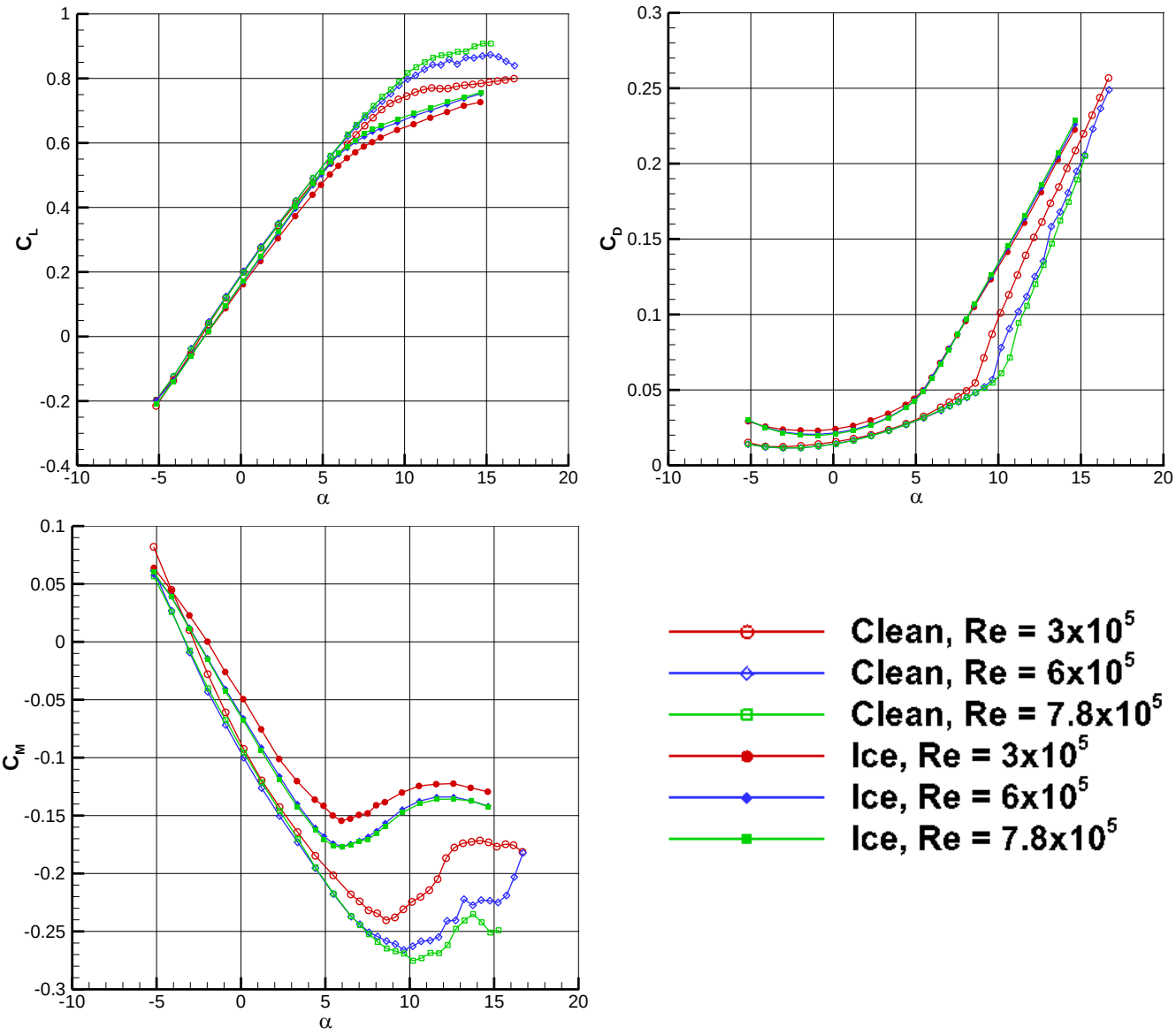

Fig. 3 Force balance results.

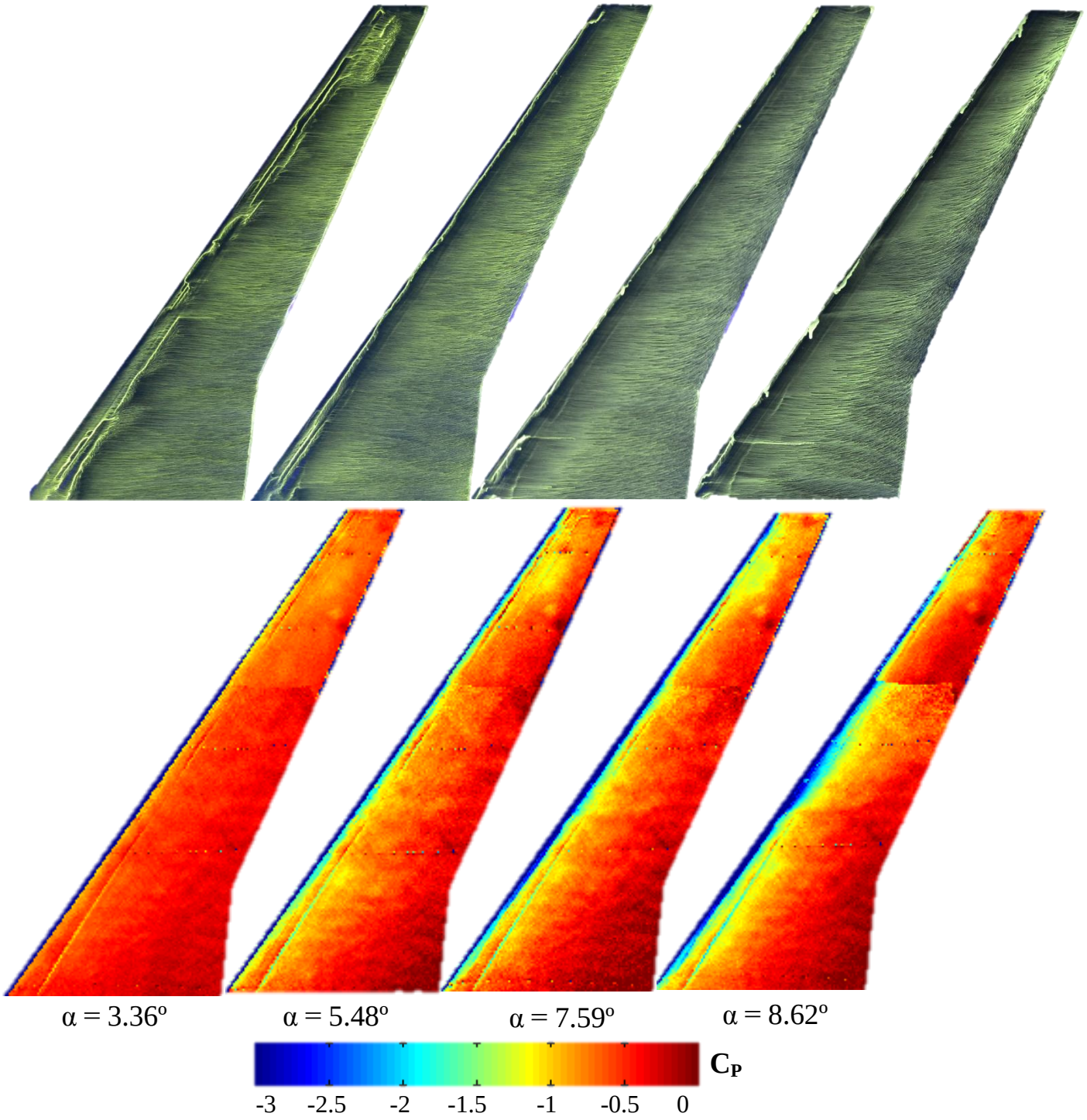

Fig. 4 Surface oil flow and pressure sensitive paint results for the clean wing at several angles of attack. Re = 6x10^5.

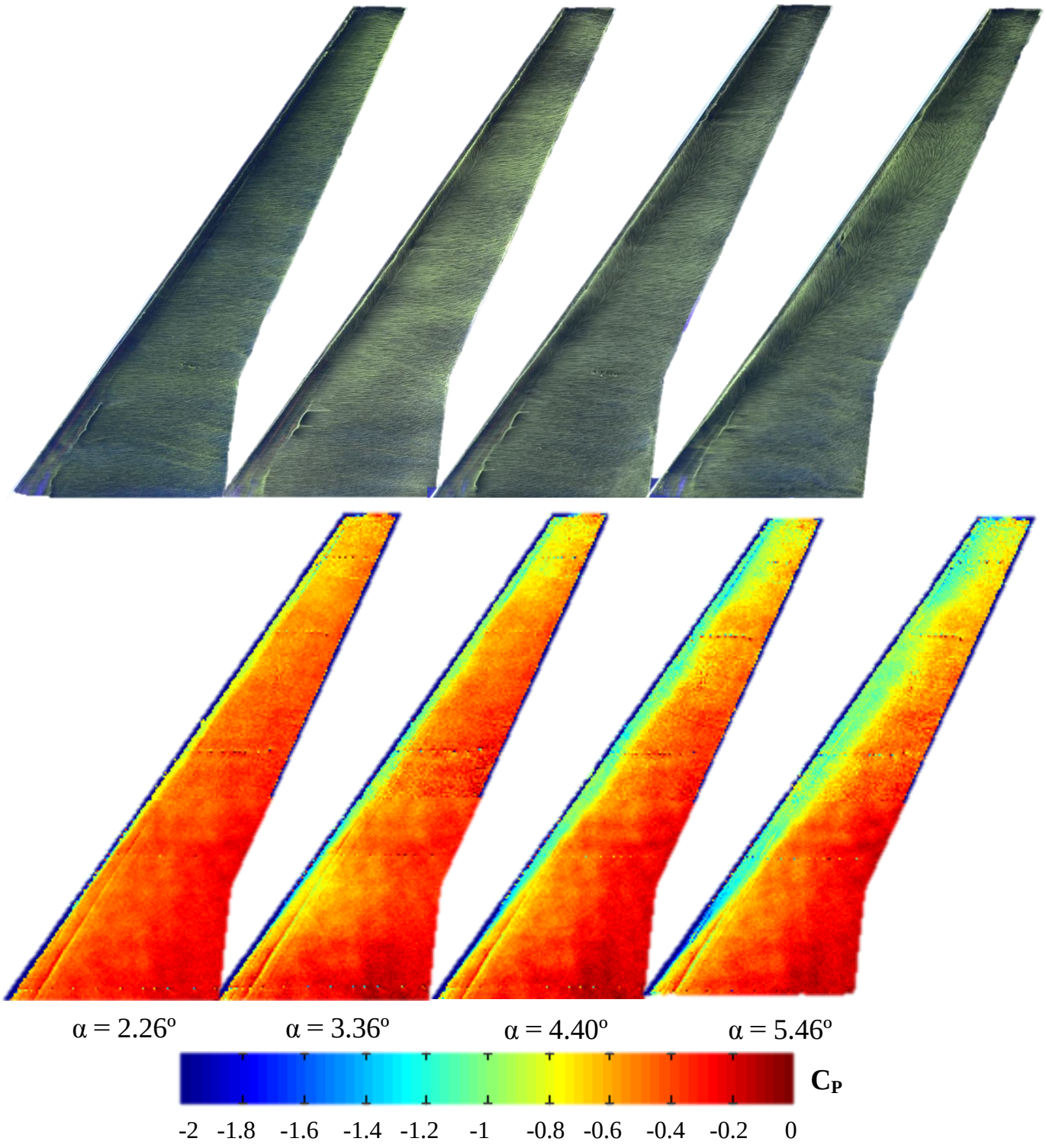

Fig. 5 Surface oil flow and pressure sensitive paint results for the iced wing at several angles of attack. Re = 6x10^5.

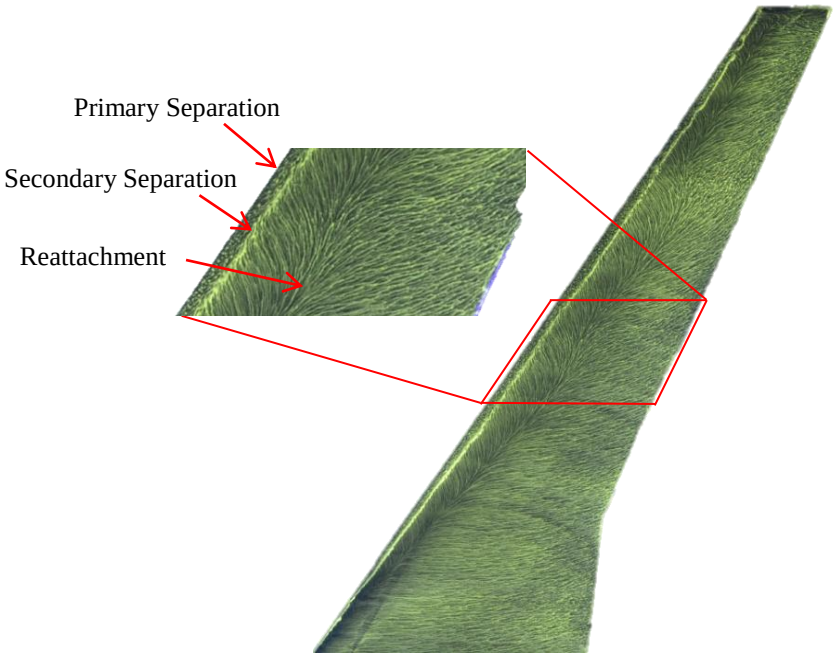

Fig. 6 Features of leading-edge vortex. Iced wing, α = 5.46°, Re = 3x10^5.

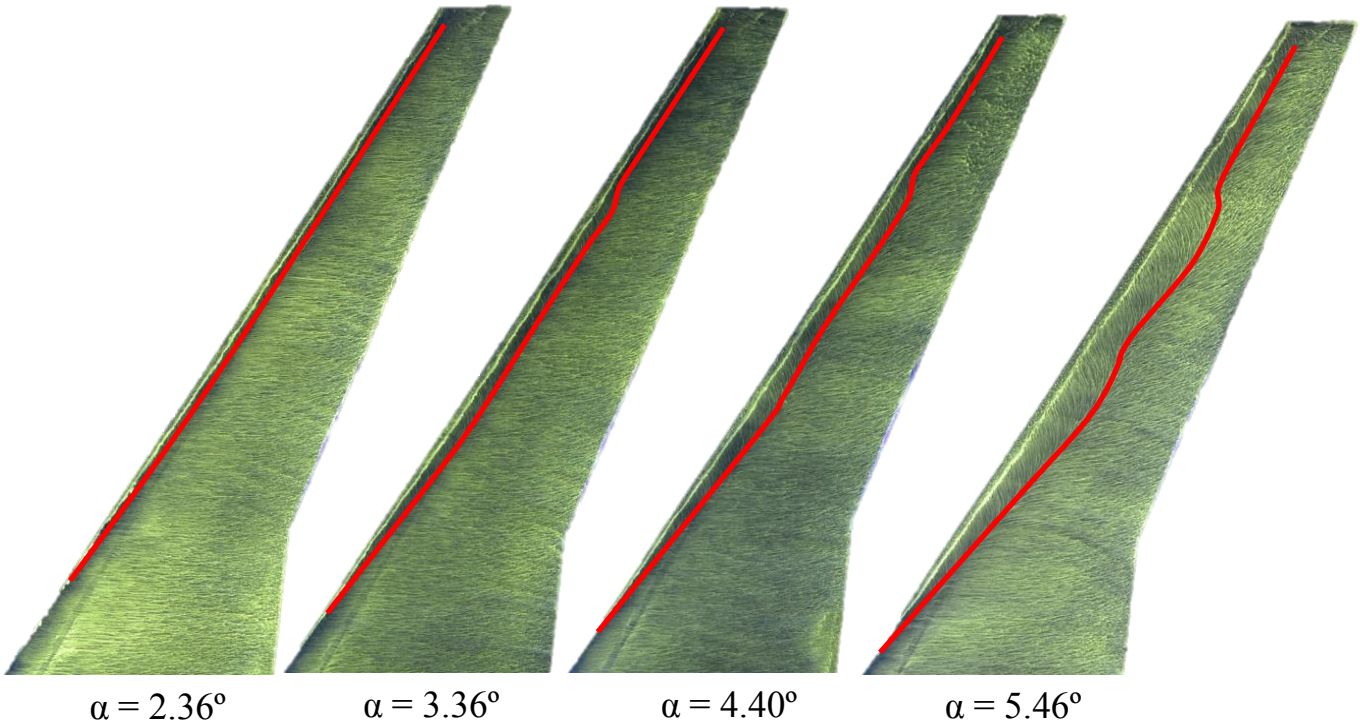

Fig. 7 Reattachment line of the separated flow on the iced wing for a range of angles. Re = 3x10^5.

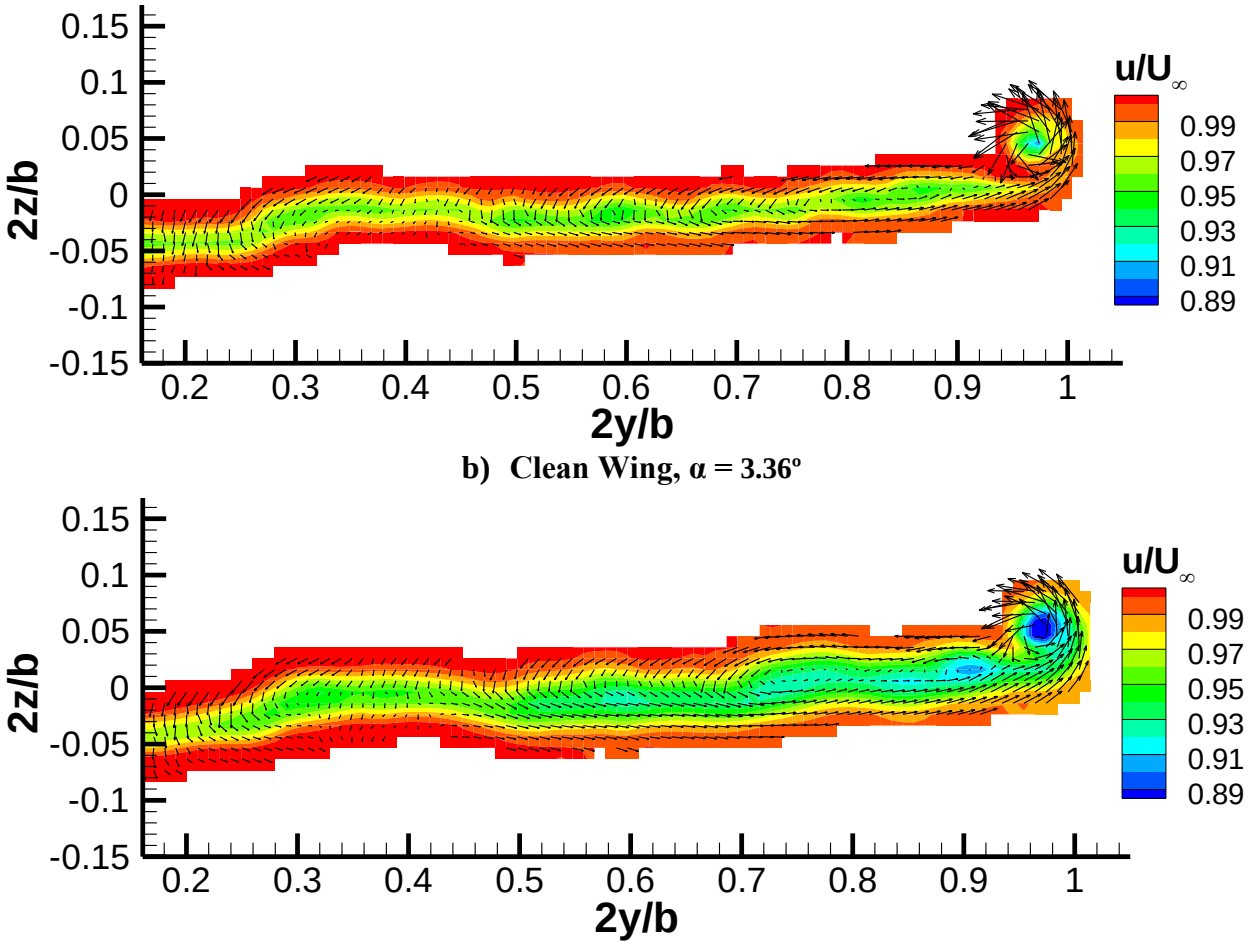

b) Clean Wing, $\alpha = 3.36^{o}$

a) Iced Wing, $\alpha = 3.36^{o}$

Fig. 8 Wakes of the a) clean wing and b) iced wings at $\alpha = 3.36^{o}$. Contours of u/U_{∞}. Vectors represent transverse velocity. Re = $6x10^{5}$.

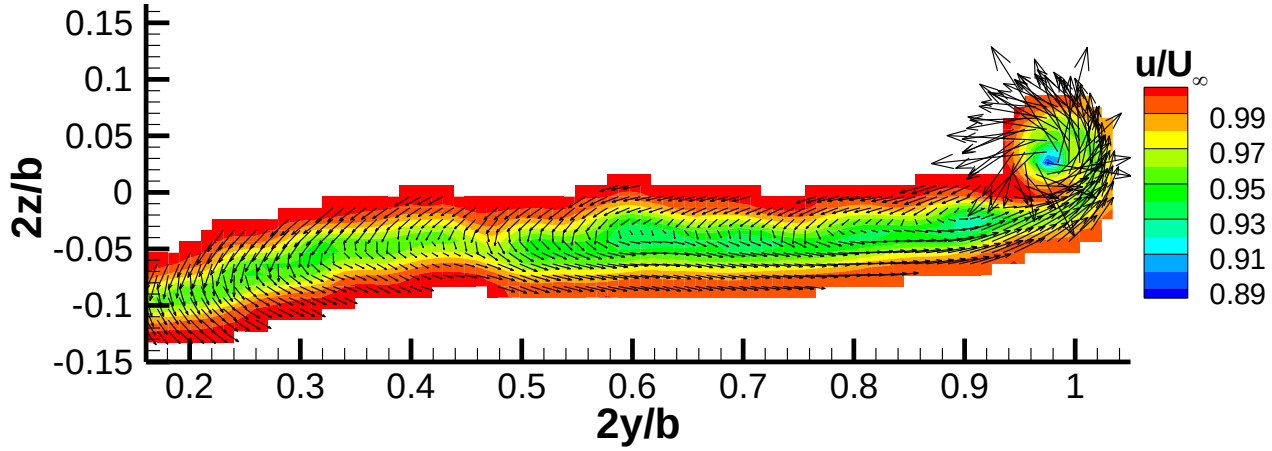

a) Clean Wing, α = 8.62°

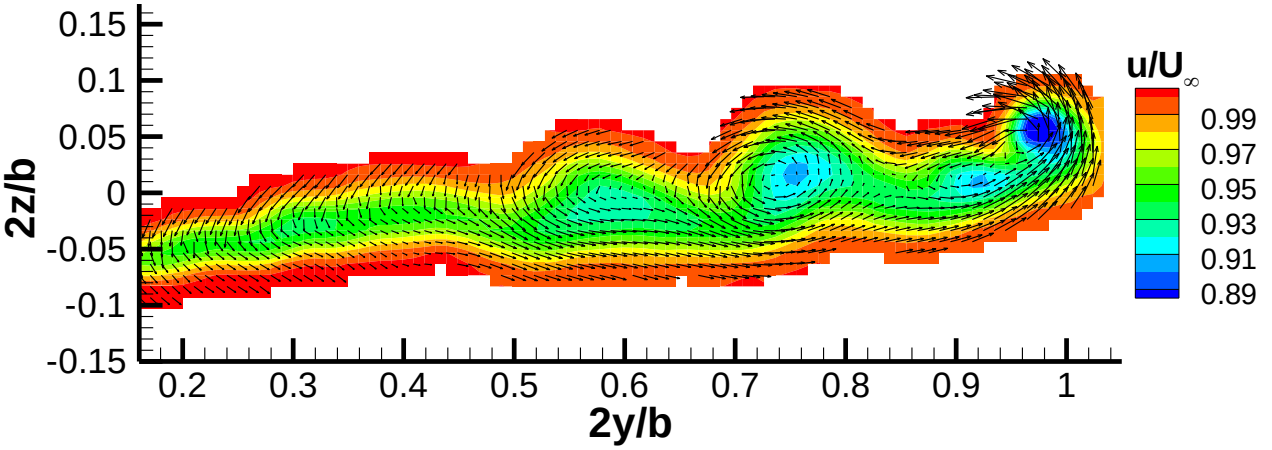

b) Iced Wing, α = 5.46°

Fig. 9 Wakes of the a) clean and b) iced wings just prior to their respective stalling angles of attack. Contours of u/U_∞. Vectors represent transverse velocity. Re = $6x10^5$.

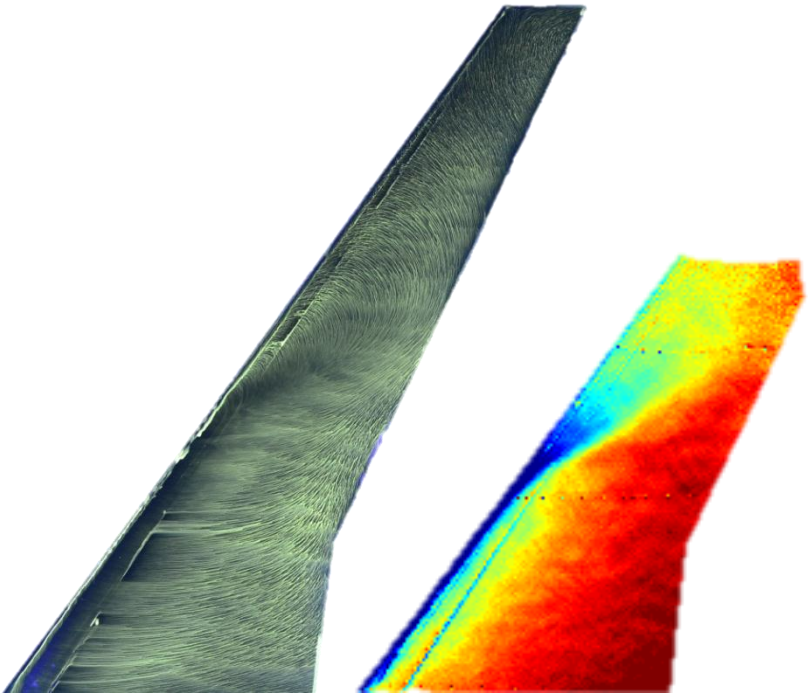

a) Clean Wing, α = 10.67°

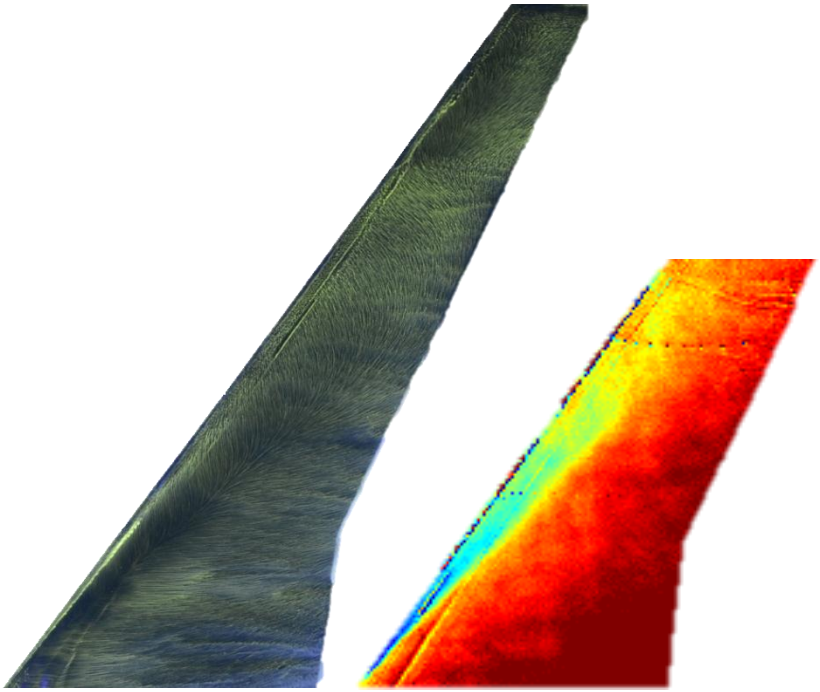

b) Iced Wing, α = 6.50°

Fig. 10 Surface oil flow visualization and PSP of a) clean and b) iced wings post stall. Re = 6x10^5.

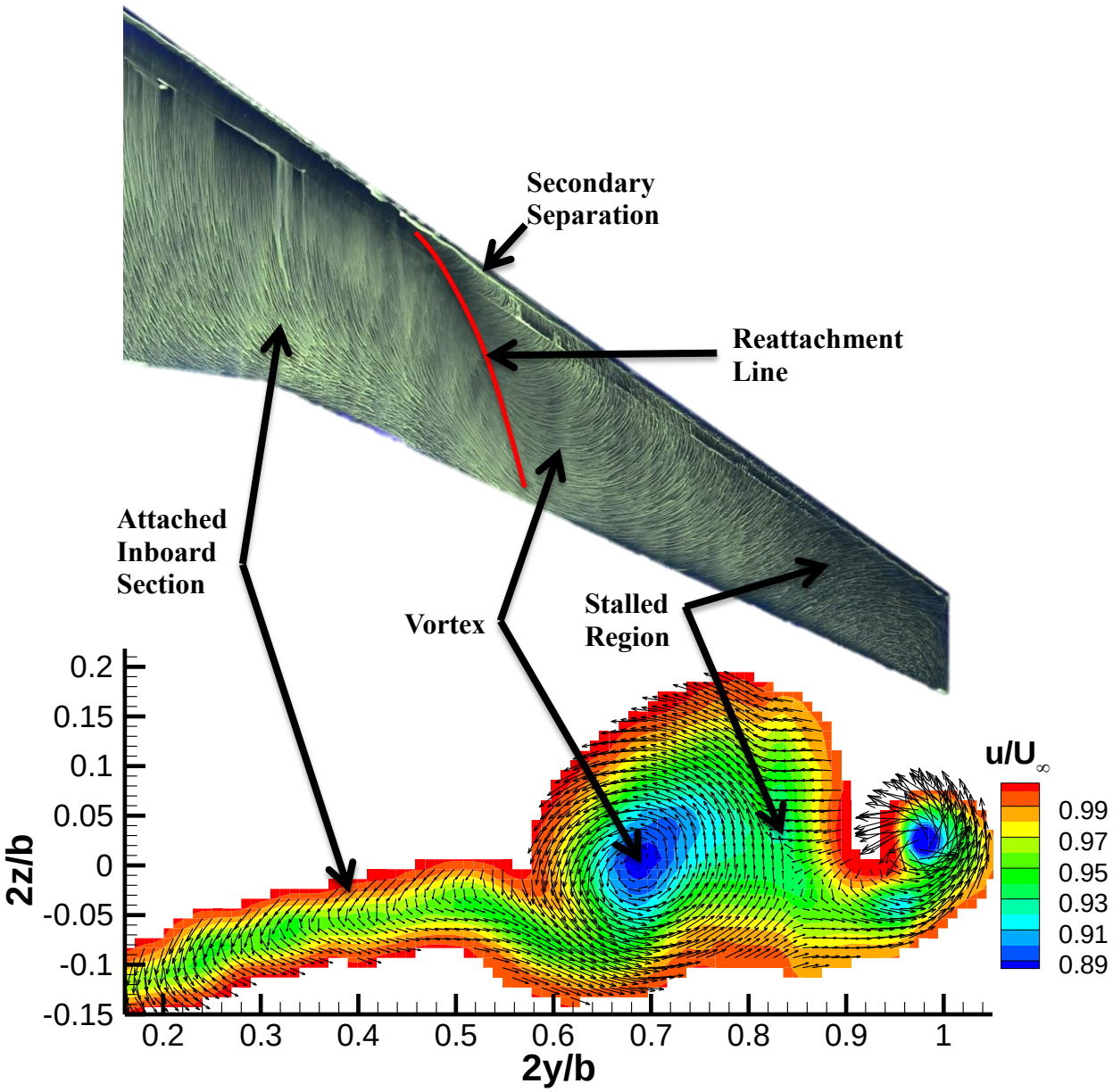

Fig. 11 Wake and oil flow of the clean wing. α = 10.67°, Re = 6x10^5.

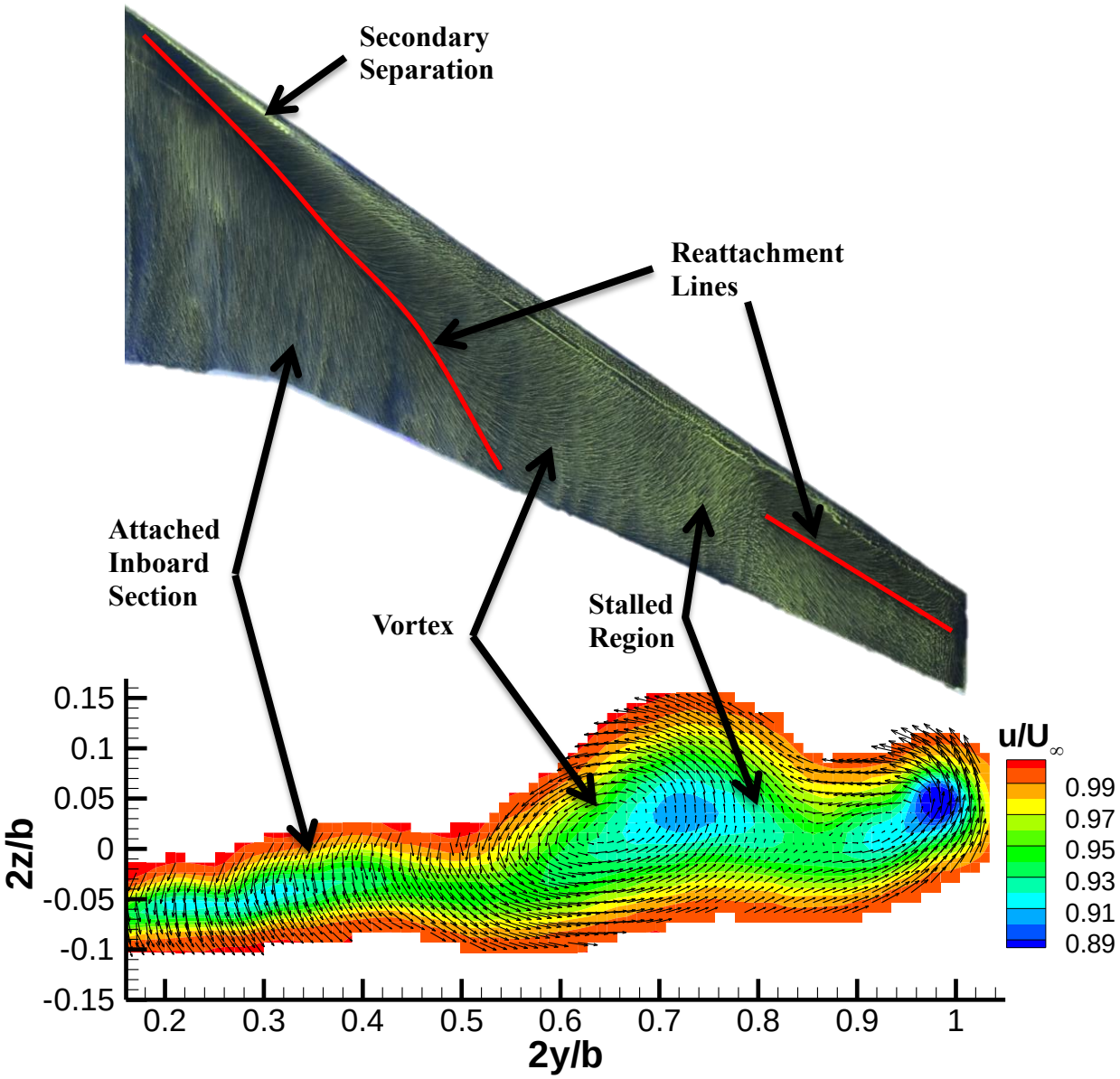

Fig. 12 Wake and oil flow of the iced wing. $\alpha = 6.50^{o}$, $Re = 6x10^{5}$.

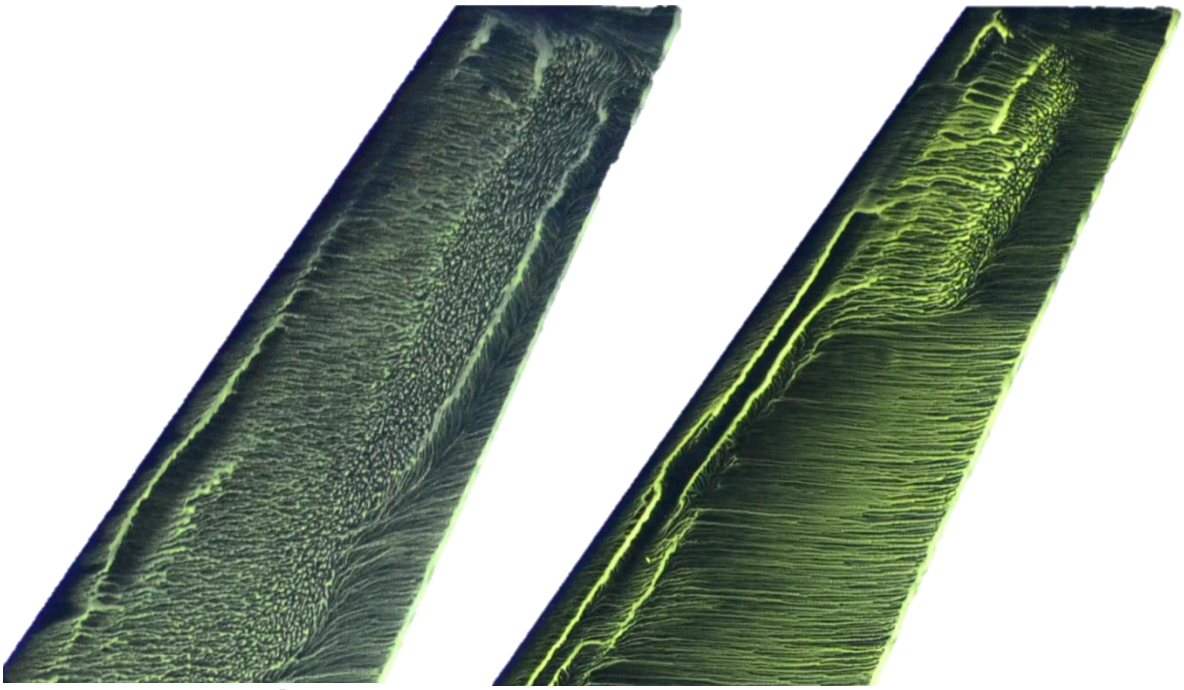

Fig. 13 Oil flow of the clean wing, 0.68 ≤ 2y/b≤ 1, at two different Reynolds numbers. α = 3.46º.

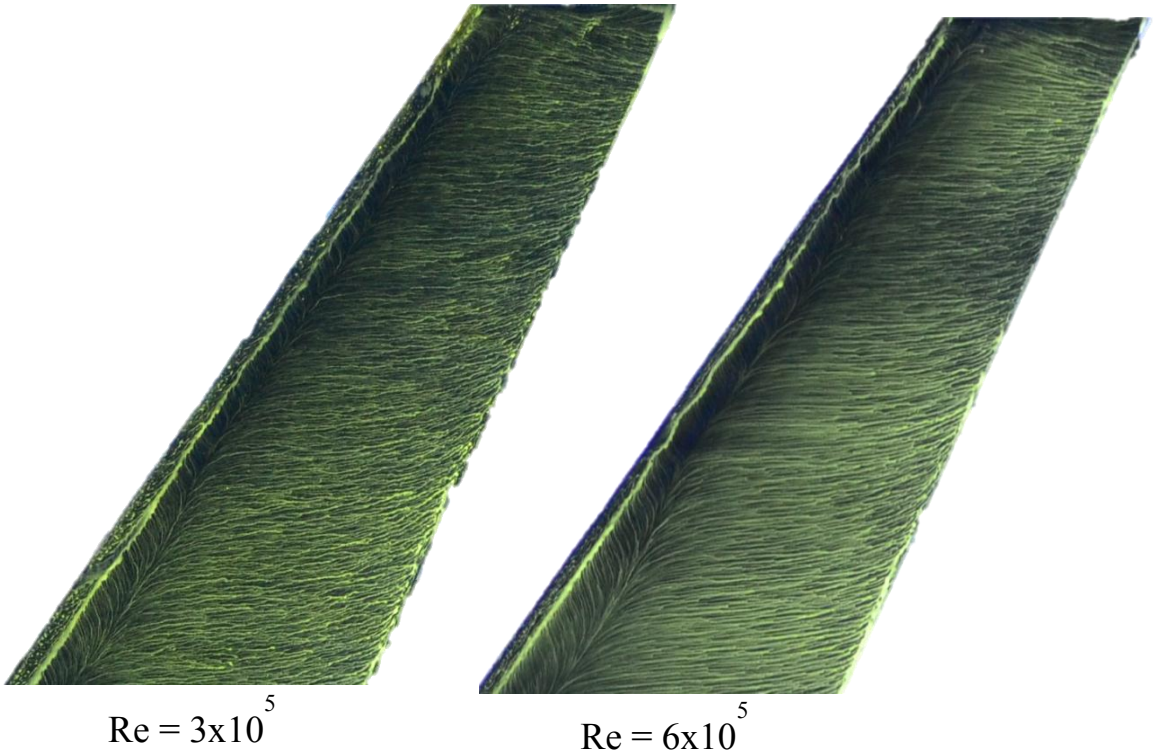

Fig. 14 Oil flow of the iced wing, 0.68 ≤ 2y/b≤ 1.0, at two different Reynolds numbers. α = 3.46º.

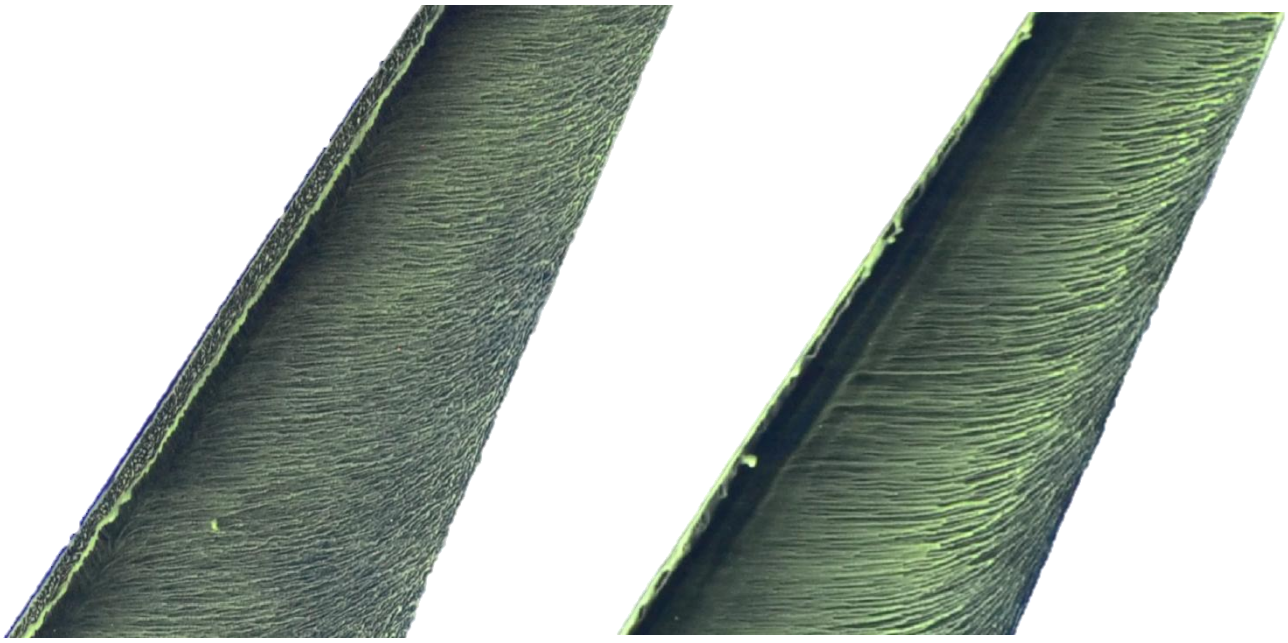

$Re = 3x10^5$ $Re = 6x10^5$

Fig. 15 Oil flow of the clean wing, 0.625 ≤ 2y/b≤ 0.925, at two different Reynolds numbers. α = 7.6º.

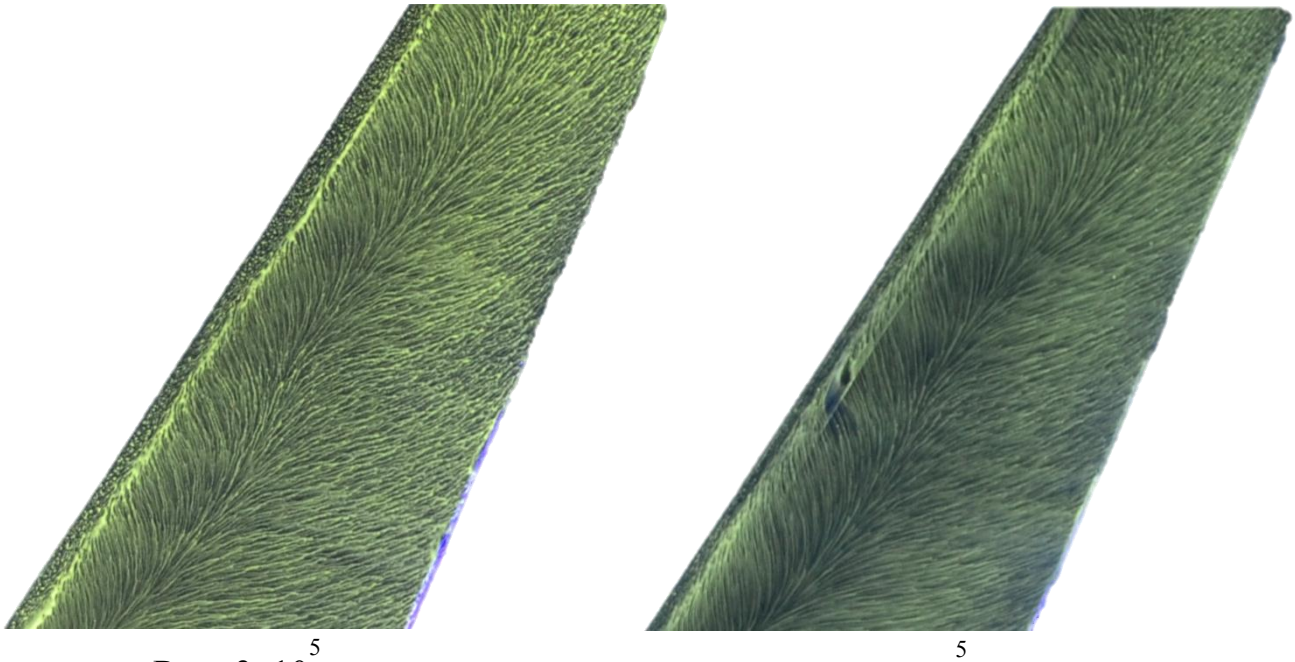

$Re = 3x10^5$ $Re = 6x10^5$

Fig. 16 Oil flow of the ice wing, 0.45 ≤ 2y/b≤ 0.75, at two different Reynolds numbers. α= 5.46º.

References

[1] Broeren, A.P., LaMarre, C.M. and Bragg, M.B. "Characteristics of SLD Ice Accretions on Airfoils and Their Aerodynamic Effects," AIAA Paper 2005-0075.

[2] Broeren, A.P., Whalen, E.A., Busch, G.T. and Bragg, M.B., "Aerodynamic Simulation of Runback Ice Accretion," AIAA 2009-4261

[3] Broeren, A.P., Bragg, M.B., Addy, H.E., Lee, S., Moens, G. and Guffond, D., "Effect of High-Fidelity Ice Accretion Simulations on Full-Scale Airfoil Performance," *Journal of Aircraft*, Vol. 47, No. 1, January-February 2010.

[4] Bragg, M.B., Broeren, A.P., and Blumenthal, L.A., "Iced-Airfoil Aerodynamics," *Progress in Aerospace Sciences* Vol. 41, p. 323-362, 2005.

[5] Lynch, F.T. and Khodadoust, A., "Effects of Ice Accretions on Aircraft Aerodynamics," *Progress in Aerospace Sciences*, Vol. 37, p. 669-767, 2001.

[6] Papadakis, M., Yeong, H.W. and Wong, S.C, "Aerodynamic Performance of a Swept Wing with Ice Accretions," AIAA 2003-0731

[7] Papadakis, M., Yeong, H.W. and Wong, S.C, "Aerodynamic Performance of a Swept Wing with Simulated Ice Shapes," AIAA 2004-0734

[8] Broeren, A.P., Lee, S., Shah, G.H. and Murphy, P.C., "Aerodynamic Effects of Simulated Ice Accretion on a Generic Transport Model," SAE Technical Paper 2011-38-0065

[9] Khodadoust, A. and Bragg, M.B., "Aerodynamics of a Finite Wing with Simulated Ice," *Journal of Aircraft* Vol. 32. No. 1., January-February 1995.

[10] Bragg, M.B., Kerho, M.F., and Khodadoust, A., "LDV Flowfield Measurements on a Straight and Swept Wing with a Simulated Ice Accretion," AIAA 1993-0300

[11] Vassberg, J.C., DeHaan, M.A., Rivers, S.M. and Wahls, R.A., "Development of a Common Research Model for Applied CFD Validation Studies," AIAA 2008-6929

[12] Potapczuk, M.G., Papadakis, M.J., and Vargas, M., "LEWICE Modeling of Swept Wing Ice Accretions," AIAA 2003-0730

[13] Meschia, F., "Model Analysis with XFLRT," *Radio Controlled Soaring Digest*, Vol. 25, No. 2, February 2008, pp. 27-51.

[14] Drela, M., "XFOIL 6.96 User Primer," MIT Aero & Astro Engineering, May 3, 2006.

[15] Barlow, J.B., W.H. Rae, J., and Pope, A., *Low Speed Wind Tunnel Testing*, John Wiley & Sons, Inc., NY, 3rd ed., 1999.

[16] Liu, T. and Sullivan, J.P., *Pressure and Temperature Sensitive Paints*, Springer, Berlin, 2005.

[17] Bell, J.H. "Applications of Pressure-Sensitive Paint to Testing at Very Low Flow Speeds," AIAA Paper 2004-878.

[18] Cattafesta III, L.N. and Moore, J.G., "Review and Application of Non-Topographic Photogrammetry to Quantitative Flow Visualization," AIAA Paper 1996-2180.

[19] Brune, G. W., "Quantitative Low Speed Wake Surveys," *Journal of Aircraft* Vol. 31, No. 2, 1994.

[20] Diebold, J., "Aerodynamics of a Swept Wing with Leading-Edge Ice at Low Reynolds Number" M.S. Thesis, Department of Aeronautical and Astronautical Engineering, University of Illinois, Urbana, IL. Expected August 2012

[21] Poll, D.I.A., "Spiral Vortex Flow Over a Swept-back Wing," Aeronautical Journal, May 1986, pp.185-199.

[22] Bragg, M.B., Khodadoust, A. and Spring, S.A., "Measurements in a Leading-edge Separation Bubble Due to a Simulated Airfoil Ice Accretion," *AIAA J.* 1992, Vol. 30, # 6, pp 1462-1467